J Mater Sci (2020) 55:8630–8641

Electronic materials

High-*k* dielectric interlayered ITO/germanium Schottky photodiodes with low dark current and high photoconductive gain

Zhiwei Huang[1], Chunyu Yu[2], Ailing Chang[2], Yimo Zhao[2], Wei Huang[2], Songyan Chen[2], and Cheng Li[2,*]

[1] *Xiamen University Tan Kah Kee College, Zhangzhou 363105, Fujian, China*
[2] *College of Physical Science and Technology, Xiamen University, Xiamen 361005, Fujian, China*

Received: 25 December 2019
Accepted: 30 March 2020
Published online:
10 April 2020

© Springer Science+Business Media, LLC, part of Springer Nature 2020

ABSTRACT

We propose a simple germanium Schottky photodiode, in which an ultrathin Al_2O_3 or HfO_2 interlayer is inserted between the indium-doped tin oxide (ITO) and *n*-Ge contact, showing low dark current and ultra-high responsivity (gain). The introduction of 2 nm thick Al_2O_3 interlayer in a ITO/*n*-Ge Schottky photodetector results in 138 × reduction of dark current, and 16 × improvement of responsivity, exhibiting a low dark current density of 32 mA/cm^2 and high responsivity of 12.5 A/W (external quantum efficiency: 1183%) for 1310 nm and 7.3 A/W (external quantum efficiency: 584%) for 1550 nm at − 4 V reverse bias, respectively. The large responsivity up to 18.5 A/W is obtained for 1310 nm at − 9 V for ITO/Al_2O_3(2 nm)/*n*-Ge diode, which corresponds to a large photoconductive gain of 24. Such a high photoconductive gain may be attributed to the capture of holes by the traps at the interface. These results are of significance for the fabrication of Ge photodetector with high performances.

Introduction

Nowadays, as tremendous growth in data traffic, silicon (Si)-based optical interconnection attracts a great research interest. In this being, photodetector is the essential link, as the photodetector is the first block of the receiver. Germanium (Ge), which like Si is group IV material, has high carrier mobility, large optical absorption coefficient at near-infrared wavelength, and fully compatible with the Si-based complementary metal–oxide–semiconductor (CMOS) process. Therefore, Ge photodetectoris regarded as one of the most promising optoelectronic devices for advanced Si photonics and optical interconnection [1–8].

High responsivity is always desirable for a photodetector. So far, most reported Ge photodetectors made with bulk Ge show responsivityof less than 1.2 A/W at 1310 and 1550 nm [7–9]. Recently, it has been confirmed that photodetectors made from Ge nanowires (NWs) with diameters ≤ 100 nm can generate extremely high responsivity in near-infrared

Address correspondence to E-mail: lich@xmu.edu.cn

https://doi.org/10.1007/s10853-020-04625-3

region [10–13]; for example, a 20 nm diameter Ge photodetector based on individual Ge nanowires with a responsivity of 22.6 A/W operating at 1550 nm wavelength have been reported [13]. However, the stringent preparation process requirements of Ge nanowires photodetectors result in a high cost. Besides, using a highly conductive and transparentindium-doped tin oxide (ITO) electrode to replace the metal electrode can reduce light reflection by metal, which would be beneficial to the improvement of responsivity [14–19].

Other than high responsivity, another desirable aspect in a photodetector is the low dark current. It has been established that the fabrication of metal–insulator semiconductor (MIS) structure can be used in low dark current photodetectors [20–22]. For metal/Ge contact, the interfacial layer between metal and Ge has the strong impact over the diode characteristics. It is reported that the dark current of Ge photodetector can be suppressed efficiently by using Ge-based MIS structure with SiO_2 as the insulating material while using high-work-function metal Pt as electrode [23]. However, the Ge-based MIS photodetectors still suffer from low responsivity at 1310 and 1550 nm. The reported Pt/SiO_2/Ge photodetector has a responsivity of only 150 and 17 mA/W for 1310 and 1550 nm, respectively. Besides, due to the small conduction band offset of 0.19 eV between ITO and Ge [24], it would be more difficult to prepare a low-dark-current Ge-based MIS photodetector with ITO as electrode.

In this work, we designed and fabricated ITO/Al_2O_3/*n*-Ge and ITO/HfO_2/*n*-Ge Schottky photodetectors to be suitable for operation in 1310 and 1550 nm wavelength. Experiments have been performed for different thickness of interlayer on lightly doped n-type Ge material to form ITO/Al_2O_3/*n*-Ge and ITO/HfO_2/*n*-Ge Schottky photodetectors. It was found that the inserting of the Al_2O_3 or HfO_2 high-*k* dielectric interlayer between ITO and *n*-Ge contact not only suppressed the dark current, but also enhanced the responsivity of the ITO/*n*-Ge Schottky photodetector. In contrast to traditional MIS photodetectors, ITO/Al_2O_3/*n*-Ge and ITO/HfO_2/*n*-Ge photodetectors show the large photoconductive gain at 1310 and 1550 nm. The possible mechanisms of the dark current suppression and photoconductive gain generation were discussed.

Experimental methods

The n-type Ge(100) wafers with a phosphorus doping concentration of 2×10^{16} cm^{-3} were firstly circularly degreased in an ultrasonic bath of acetone, ethanol, and deionized water, then immersed in a dilute hydrofluoric acid solution (HF: H_2O = 1: 50) to remove the native oxide, finally rinsed with deionized water, and blown dry with nitrogen. After cleanout, the wafers were loaded into atomic layer deposition (ALD) system, Al_2O_3 or HfO_2 film with various thicknesses (0–3 nm) was deposited on the *n*-Ge. Next, the wafers were immediately loaded into a well-controlled sputtering system, and a shadow mask with circular patterns was fixed on the front side of the Al_2O_3/*n*-Ge and HfO_2/*n*-Ge samples, followed by deposition of 100-nm-thick ITO on the samples to form contacts with an area of 0.0003 cm^2. The samples without high-*k* dielectric interlayer were also prepared for comparison. Finally, 300 nm of Al was deposited on the backside of all the samples by DC magnetron sputtering as the other electrode.

The Al_2O_3 layer was deposited by ALD at 200 °C using Trimethylaluminium($Al(CH_3)_3$) and H_2O as precursors. The HfO_2 layer was deposited by ALD at 275 °C using tetrakis (ethyl methylamino) hafnium ($Hf[N(CH_3)(C_2H_5)]_4$) and H_2O as precursors. The ITO films were deposited at a DC power of 33 W onto a 60-mm-diameter target (purity: 99.99%, In_2O_3: SnO_2 = 90: 10 wt %) under Ar ambient at 0.3 Pa and room temperature with a deposition rate of 0.08 nm/s. The Al films were deposited at a DC power of 112 W onto a 60-mm-diameter Al target under Ar ambient at 0.5 Pa and room temperature with a deposition rate of 0.15 nm/s.

The surface morphology was analyzed by atom force microscopy (AFM, Seiku Instruments, and SPI4000/SPA-400) in a tapping mode. The chemical states of the interlayers on the Ge surface were evaluated by X-ray photoelectron spectroscopy (XPS, Quantra/Quantum 2000 Scaning ESCA Microprobe). The cross-sectional image of ITO/*n*-Ge and ITO/Al_2O_3/*n*-Ge is characterized by transmission electron microscopy (JEM2100). The current–voltage (*I*–*V*) characteristics were acquired by a Keithley 2611B source/meter.

Results and discussions

The atomic force microscopy (AFM) images with a scanned area of 10 × 10 μm^2 of clean bare *n*-Ge, Al_2O_3(3 nm)/*n*-Ge and HfO_2(3 nm)/*n*-Ge are shown in Fig. 1. The surface of the 3-nm-thick Al_2O_3 or HfO_2 film on Ge is very smooth, and the root-mean-square (RMS) surface roughness is just 0.5 nm (Fig. 1b) and 0.4 nm (Fig. 1c), respectively, which are comparable to clean bare Ge (Fig. 1a). The great smoothness of the Al_2O_3 and HfO_2 films can provide a uniform ultrathin interlayer between ITO and *n*-Ge to form ITO/Al_2O_3/*n*-Ge or ITO/HfO_2/*n*-Ge photodiodes.

The room-temperature dark *I*–*V* characteristics of the ITO/Al_2O_3/*n*-Ge and ITO/HfO_2/*n*-Ge photodiodes with various thicknesses (0–3 nm) interlayer are shown in semi-log plots in Fig. 2a, b, respectively. Overall, the *I*–*V* curve shows rectifying current characteristics for each device. However, their rectifying behaviors exhibit different features. As can be seen, the rectifying ratio of the *I*–*V* curve increased markedly, whereas the reverse dark current decreased for both ITO/Al_2O_3/*n*-Ge and ITO/HfO_2/*n*-Ge diodes, compared with that of the ITO/*n*-Ge diode. Figure 2c, d shows the changes of the reverse current at − 1 V bias voltage and forward current at +1 V bias voltage for ITO/Al_2O_3/*n*-Ge and ITO/HfO_2/*n*-Ge diodes with various thicknesses interlayer from 0 to 3 nm. It is clearly shown that the reverse current decreased significantly after the Al_2O_3 or HfO_2interlayer is introduced. Specifically, a well-behaved ITO/Al_2O_3(2 nm)/*n*-Ge Schottky diode with a high rectification ratio (± 1 V) of ~ 2.6 × 10^3 and low dark current (− 1 V) of 2.4 × 10^{-6} A is achieved. Such dark current is 260 × lower than the ITO/*n*-Ge diode. Besides, it should also be noted that the introduction of Al_2O_3 or HfO_2 interlayer can lead to the decrease of forward current. The introduction of Al_2O_3 or HfO_2 layer was able to increase the Schottky barrier height of ITO/*n*-Ge, leading to a reduction of the dark current. However, a too thick high-*k* layer would inevitably introduce extra resistance, which would worsen the responsivity of diodes. Given that, the thickness of high-*k* layer should not be too thick.

The enhancement of rectifying ratio of the *I*–*V* curve implies the increase of electron Schottky barrier height (Φ_{SBH}) in the diodes. Take ITO/Al_2O_3/*n*-Ge diodes, for example. To quantitatively evaluate Φ_{SBH} values of the ITO/Al_2O_3/*n*-Ge diodes, we measured and analyzed the temperature-dependent current density–voltage (*J*–*V*) characteristics. In this work, the doping concentration of *n*-Ge substrate is just 2 × 10^{16} cm^{-3}, and the *J*–*V* characteristics of diodes were measured at temperatureabove 300 k. In this condition, the ratio of tunneling current to thermionic current would be much less than 1 for the Schottky diode [25]. Given that, the height of Schottky barrier of ITO/Al_2O_3/*n*-Ge diodes was extracted just according to the thermionic emission theory, without considering the tunneling process.

Figure 3a, b shows the temperature-dependent *J*–*V* characteristics of ITO/*n*-Ge and ITO/Al_2O_3(2 nm)/*n*-Ge diode, respectively. The Φ_{SBH} of the diodes could be extracted from temperature-dependent *J*–*V* characteristics using the activation energy method [26]. The well linear correlation for extracted ln(J/T^2) versus 1000/T Richardson plots for ITO/Al_2O_3/*n*-Ge

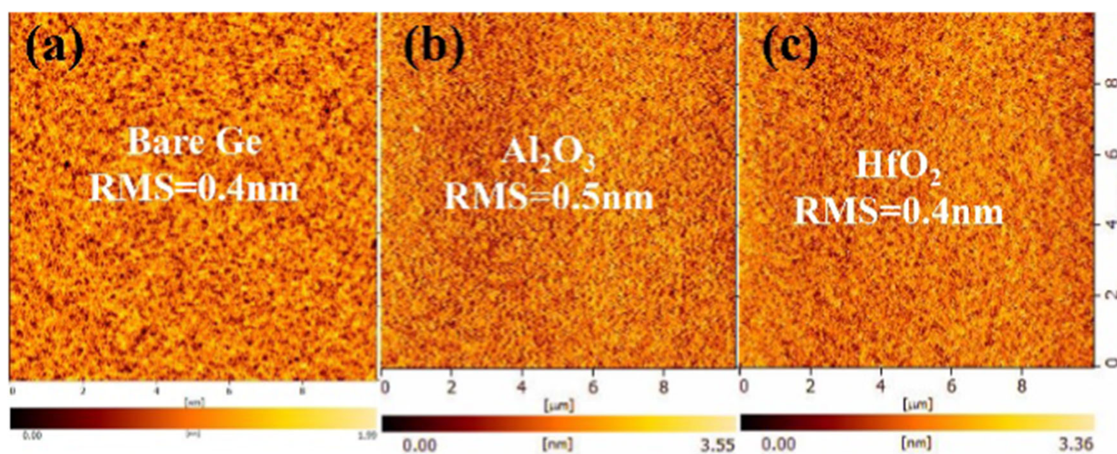

Figure 1 The AFM images with a scanned area of 10 × 10 μm^2 of **a** clean bare *n*-Ge, **b** Al_2O_3(3 nm)/*n*-Ge and **c** HfO_2(3 nm)/*n*-Ge.

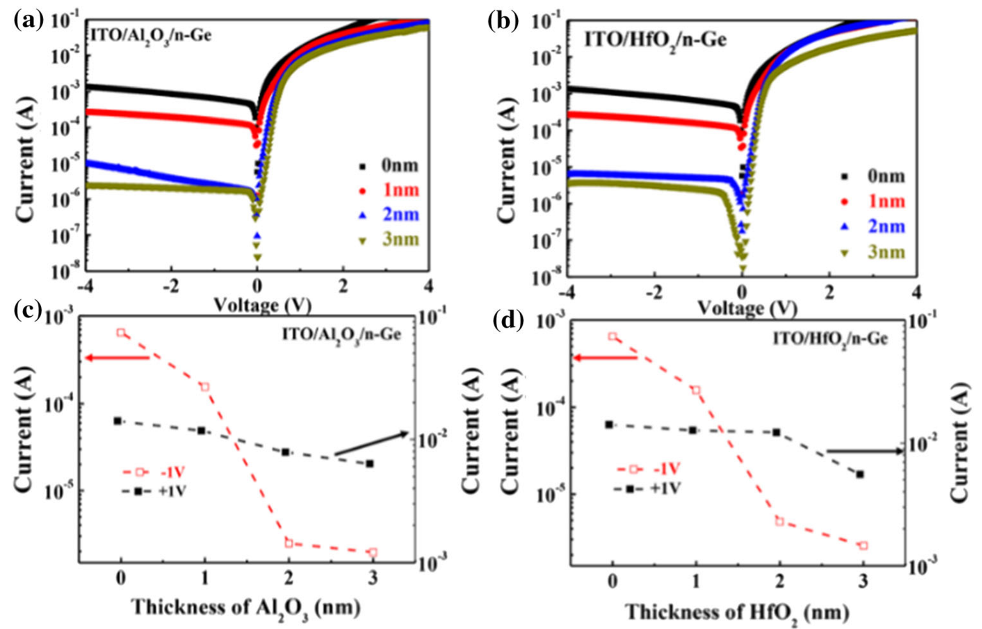

Figure 2 Room-temperature *I–V* characteristics of the **a** ITO/Al_2O_3/*n*-Ge and **b** ITO/HfO_2/*n*-Ge diodes with various thicknesses interlayer. Dependence of forward and reverse current densities at ± 1 V bias voltage for **c** ITO/Al_2O_3/*n*-Ge and **d** ITO/HfO_2/*n*-Ge diodes on interlayer thickness.

diodes with varying Al_2O_3 interlayer thickness can be seen in Fig. 3c. As shown in Fig. 3d, the extracted effective Φ_{SBH} of ITO/Al_2O_3/*n*-Ge diodes increases with increase of Al_2O_3 thickness. An extracted effective Φ_{SBH} up to 0.59 eV is achieved for the ITO/Al_2O_3(3 nm)/*n*-Ge diode, 0.34 eV higher than of the ITO/*n*-Ge control device, as shown in Fig. 3d.

It has been confirmed that the interfacial layer between ITO and *n*-Ge has the strong impact over the diode characteristics and the effective Φ_{SBH}. To take a closer look to the sample interfaces, the typical cross-sectional transmission electron microscopy (TEM) images of ITO/*n*-Ge and ITO/Al_2O_3(2 nm)/*n*-Ge structures were measured, as shown in Fig. 4.

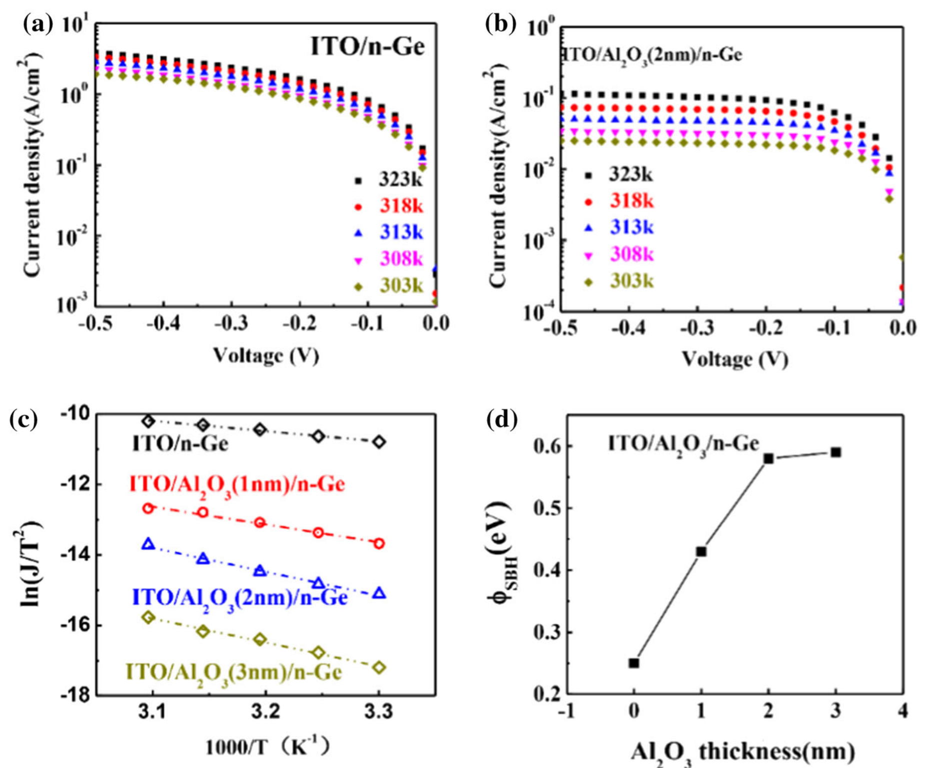

Figure 3 Temperature-dependent *J–V* characteristics of **a** ITO/*n*-Ge and **b** ITO/Al_2O_3(2 nm)/*n*-Ge diode. **c** $\ln(J/T^2)$ versus 1000/T for ITO/Al_2O_3/*n*-Ge diodes, and **d** the extracted effective Φ_{SBH} for varying Al_2O_3 interlayer thickness.

Figure 4a, b displays the cross-sectional TEM of ITO/*n*-Ge structure. It is reported that Ge atoms can be oxidized when ITO was deposited onto a heated (300 °C) Ge substrate under Ar/O_2 (50/1) ambient, in which the presence of GeO_x at the interface of the ITO and Ge was observed by TEM image [19]. However, in this work, ITO was deposited onto a Ge substrate under high-purity Ar ambient at room temperature. Thus, the oxidation reaction of Ge surface should be slight in the sputtered deposition of ITO. Figure 4a reveals that the ITO layer is uniform, and the film thickness of ITO was estimated about 100 nm. Besides, there is not obvious middle layer exist between the ITO and Ge substrate as shown in Fig. 4b. Figure 4c, d displays the cross-sectional TEM of ITO/Al_2O_3(2 nm)/*n*-Ge structure. Figure 4c reveals that the ITO layer and Al_2O_3 interlayer are uniform, and the interfaces among ITO electrode, Al_2O_3 interlayer and *n*-Ge substrate are clear and smooth. The thickness of Al_2O_3 interlayer was estimated about 2 nm as shown in Fig. 4d.

To evaluate the chemical states of the oxides on the Ge surface, XPS measurements were carried out for Al_2O_3(2 nm)/*n*-Ge and HfO_2(2 nm)/*n*-Ge samples as shown in Fig. 5. For the XPS spectra on the surface of Al_2O_3(2 nm)/*n*-Ge sample, the binding energy of 74.50 eV is well fitted in Al 2*p* XPS spectra as depicted in Fig. 5a, corresponding to the oxidation state of Al_2O_3 [27]. As shown in Fig. 5b, the Ge 3*d* XPS peak of Al_2O_3(2 nm)/*n*-Ge sample centered at 29.88 eV corresponds to the bulk Ge, and the chemical shift of 1.63 eV to the bulk Ge indicates the existence of Ge suboxides [28] which may be originated from oxidation of Ge in ALD system. For HfO_2(2 nm)/*n*-Ge sample, the doublet peaks with binding energy of 17.1 eV and 18.75 eV are well fitted in the Hf 4*f* XPS spectra as depicted in Fig. 5c, corresponding to Hf–O bonds [29]. The chemical shift between bulk Ge and GeO_x is about 2.50 eV in Ge 3*d* XPS spectra as shown in Fig. 5d, which also indicates the existence of Ge suboxides.

The barrier height between ITO and *n*-Ge is determined by conduction band offsets (ΔEc) between ITO and *n*-Ge, and is also affected by

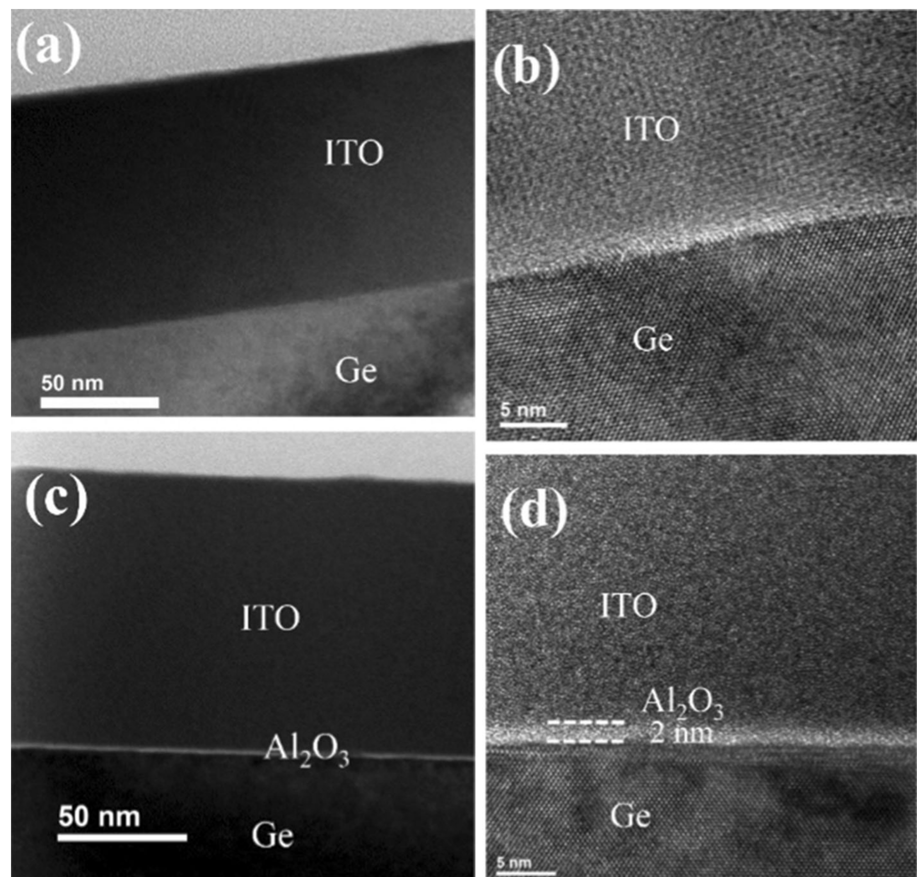

Figure 4 Cross-sectional TEM images of **a**, **b** ITO/*n*-Ge and **c**, **d** ITO/Al_2O_3(2 nm)/*n*-Ge structures.

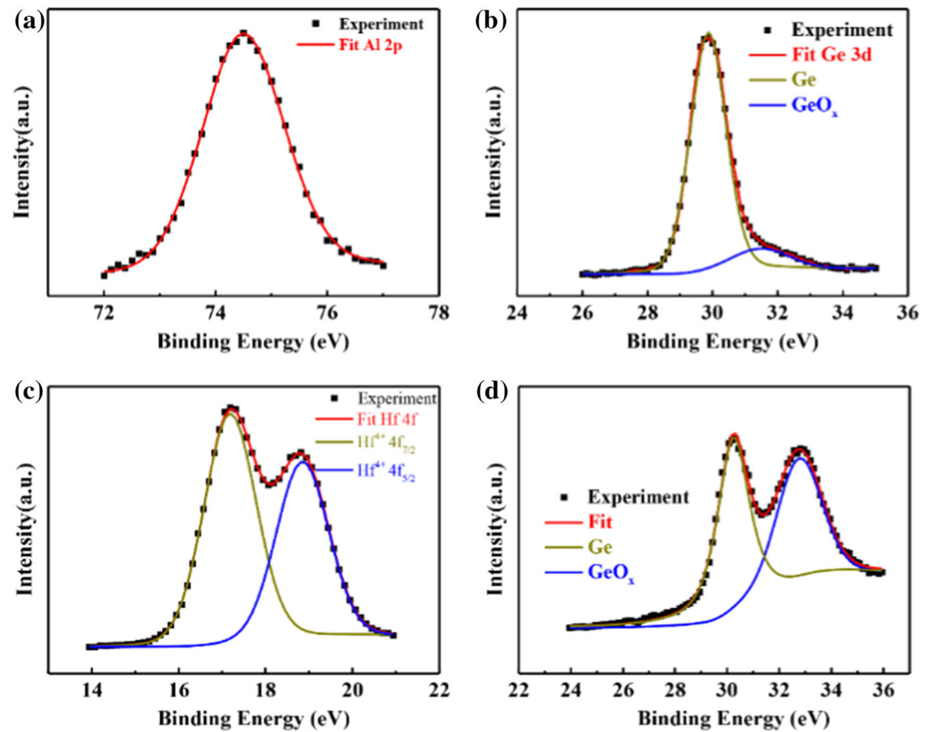

Figure 5 XPS spectra of **a** Al 2*p* and **b** Ge 3*d* for Al_2O_3(2 nm)/*n*-Ge sample. XPS spectra of **c** Hf 4*f* and **d** Ge 3*d* for HfO_2(2 nm)/*n*-Ge sample.

interface states between ITO and *n*-Ge. A low barrier height has been obtained for the ITO/*n*-Ge diode due to the small ΔEc between ITO and Ge, suggesting the small interface state density between ITO and Ge. By contrast, high Φ_{SBHs} have been obtained for ITO/Al_2O_3/*n*-Ge and ITO/HfO_2/*n*-Ge diodes, suggesting the high interface state density. At a metal–semiconductor contact, when considering the effect of interface state, the Schottky contact barrier height Φ_{SBH} can be described by [30]:

$$\phi_{SBH} = S(\Phi_m - \Phi_{CNL}) + (\Phi_{CNL} - \chi_S) \quad (1)$$

where S is the pinning factor, Φ_m is the metal work function, Φ_{CNL} and χ_S is the semiconductor charge neutrality level and electron affinity, respectively. For ITO/Al_2O_3/*n*-Ge or ITO/HfO_2/*n*-Ge diodes, it is considered that the instability of Ge suboxides can lead to abundant dangling bonds on the Ge surface, resulting in strong Fermi-level pinning (FLP) [31], which means a low pinning factor S ($\sim$ 0). Besides, it is reported that the charge neutrality level in Ge is 0.1 eV above its valence band [32]. Those should be responsible for the high Φ_{SBH} of ITO/Al_2O_3/*n*-Ge and ITO/HfO_2/*n*-Ge diodes.

The introduction of an Al_2O_3 or HfO_2 interlayer has been demonstrated to effectively decrease the dark current for ITO/*n*-Ge diodes. In order to investigate the responsivity of ITO/Al_2O_3/*n*-Ge device to the incident light, the photoresponse of the device was measured at reverse bias for wavelength of 1310 and 1550 nm. The photocurrents of the ITO/Al_2O_3(1 nm)/*n*-Ge, ITO/Al_2O_3(2 nm)/*n*-Ge and ITO/Al_2O_3(3 nm)/*n*-Ge diodes measured under illumination with a 1310 nm laser at various powers are shown in Fig. 6a–c, respectively. Overall, the photocurrents of ITO/Al_2O_3(2 nm)/*n*-Ge and ITO/Al_2O_3(3 nm)/*n*-Ge diodes are larger than the photocurrents of ITO/Al_2O_3(1 nm)/*n*-Ge diode under the same test conditions. Besides, it is shown that the photocurrents of ITO/Al_2O_3(1 nm)/*n*-Ge diode linear increases, while the photocurrents of ITO/Al_2O_3(2 nm)/*n*-Ge and ITO/Al_2O_3(3 nm)/*n*-Ge diodes gradually approach a saturated value as laser power increases.

Figure 6d, e show the responsivities of ITO/Al_2O_3(1 nm)/*n*-Ge, ITO/Al_2O_3(2 nm)/*n*-Ge and ITO/Al_2O_3(3 nm)/*n*-Ge diodes measured at − 2, − 3 and − 4 V bias under illumination with a 1310 nm laser at various powers. As shown in Fig. 6d, the responsivity of ITO/Al_2O_3(1 nm)/*n*-Ge is less related to the reverse bias and power of laser. At − 4 V reverse bias, the ITO/Al_2O_3(1 nm)/*n*-Ge diode approaches to a saturated responsivity of 0.76 A/W for 1310 nm laser at a power of 1.0 mW. The responsivities of ITO/Al_2O_3(2 nm)/*n*-Ge and ITO/Al_2O_3(3 nm)/*n*-Ge

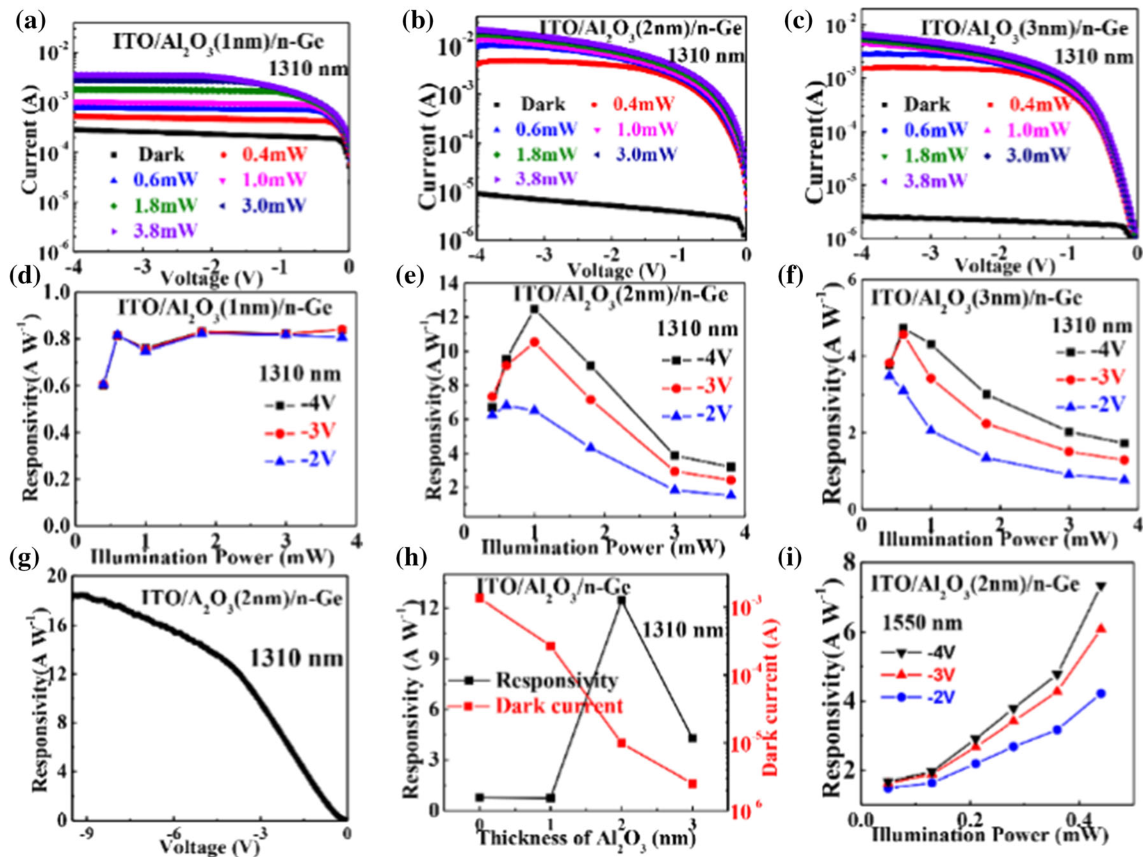

Figure 6 Photocurrent of the **a** ITO/Al_2O_3(1 nm)/*n*-Ge, **b** ITO/Al_2O_3(2 nm)/*n*-Ge and **c** ITO/Al_2O_3(3 nm)/*n*-Ge diodes measured under illumination by a 1310 nm laser at different powers. The responsivities of **d** ITO/Al_2O_3(1 nm)/*n*-Ge, **e** ITO/Al_2O_3(2 nm)/*n*-Ge and **f** ITO/Al_2O_3(3 nm)/*n*-Ge diodes measured at − 2, − 3 and − 4 V reverse bias under illumination by a 1310 nm laser at various powers. **g** Dependence of responsivity of the ITO/Al_2O_3(2 nm)/*n*-Ge diode on reverse bias voltage. **h** Dependence of dark current and responsivity (at 1310 nm) of the ITO/Al_2O_3/*n*-Ge diodes on Al_2O_3 thickness from 0 to 3 nm. **i** Dependence of responsivity of ITO/Al_2O_3(2 nm)/*n*-Ge diode on power of a 1550 nm laser.

diodes, in contrast, show more closely correlated with the reverse bias and power of laser. As show in Fig. 6e, the responsivity of ITO/Al_2O_3(2 nm)/*n*-Ge diode increases with increasing reverse bias; meanwhile, the responsivity of ITO/Al_2O_3(2 nm)/*n*-Ge diode firstly increases and then decreases with increasing the laser power. Specifically, a high responsivity of 12.5 A/W (external quantum efficiency: 1183%) for 1310 nm at a power of 1.0 mW is achieved for ITO/Al_2O_3(2 nm)/*n*-Ge diode at − 4 V reverse bias, corresponding to a large photoconductive gain of 16. In general, the variation tendency of the photocurrents and responsivity of ITO/Al_2O_3(3 nm)/*n*-Ge diode is analogous to ITO/Al_2O_3(2 nm)/*n*-Ge diode. However, compared with ITO/Al_2O_3(2 nm)/*n*-Ge diode, the responsivity of ITO/Al_2O_3(3 nm)/*n*-Ge diode becomes smaller by about three times, as shown in Fig. 6f.

Figure 6g shows the dependence of responsivity of the ITO/Al_2O_3(2 nm)/*n*-Ge diode on reverse bias voltage from 0 to − 9 V measured under illumination by a 1310 nm laser at 1.0 mW. The responsivity of the ITO/Al_2O_3(2 nm)/*n*-Ge diode increases gradually with the increase of reverse bias voltage. At − 9 V, a high responsivity of 18.5 A/W (corresponding to a large photoconductive gain of 24) for 1310 nm at a power of 1.0 mW is achieved for ITO/Al_2O_3(2 nm)/*n*-Ge diode. Figure 6h shows the dependence of dark current (at − 4 V bias) and responsivity (at − 4 V bias with 1310 nm laser at a power of 1.0 mW) of the ITO/Al_2O_3/*n*-Ge diodes on the thickness of Al_2O_3 from 0 to 3 nm. It is clearly shown that the dark current decreases significantly with increase of Al_2O_3 thickness, the introduction of 2 nm and 3 nm thick Al_2O_3 interlayer in a ITO/*n*-Ge Schottky photodetector results in 138 × and 544 × reduction of dark

current respectively, exhibiting a low dark current density of 32 mA/cm^2 and 8.3 mA/cm^2 respectively. Meanwhile, the responsivity of ITO/Al_2O_3/*n*-Ge diodes first increases and then decreases with increasing Al_2O_3 thickness. Figure 6i shows the responsivity of ITO/Al_2O_3(2 nm)/*n*-Ge diode measured at − 2, − 3 and − 4 V reverse bias under illumination by a 1550 nm laser at various powers. The responsivity of ITO/Al_2O_3(2 nm)/*n*-Ge diode increases with increasing reverse bias or increasing the power (0–0.4 mW) of laser at 1550 nm wavelength. At − 4 V reverse bias, a high responsivity of 7.3 A/W (external quantum efficiency: 584%) for 1550 nm at a power of 0.4 mW is achieved for the ITO/Al_2O_3(2 nm)/*n*-Ge diode.

The photocurrent of the ITO/HfO_2(1 nm)/*n*-Ge, ITO/HfO_2(2 nm)/*n*-Ge and ITO/HfO_2(3 nm)/*n*-Ge diodes measured under illumination by a 1310 nm laser at various powers are shown in Fig. 7a, c, respectively. Figure 7d, e shows the responsivities of ITO/HfO_2(1 nm)/*n*-Ge, ITO/HfO_2(2 nm)/*n*-Ge and ITO/HfO_2(3 nm)/*n*-Ge diodes measured at − 2, − 3 and − 4 V reverse bias under illumination by a 1310 nm laser at various powers. Overall, the variation tendency of the photocurrents and responsivity of ITO/HfO_2/*n*-Ge diodes are analogous to ITO/Al_2O_3/*n*-Ge diodes. The phenomena of photoconductive gain can be also observed for ITO/HfO_2(2 nm)/*n*-Ge and ITO/HfO_2(3 nm)/*n*-Ge diodes.

For further comparison, Fig. 8a shows the comparison of dark currents and photocurrents measured under illumination with a 1310 nm laser at power of 1 mW for ITO/*n*-Ge, ITO/Al_2O_3(2 nm)/*n*-Ge and ITO/HfO_2(2 nm)/*n*-Ge diodes. It is shown that a poor distinguish ability between photo and dark current is observed for the ITO/*n*-Ge diode owing to its high dark current and low responsivity. The ITO/Al_2O_3(2 nm)/*n*-Ge and ITO/HfO_2(2 nm)/*n*-Ge diodes, by contrast, show better photoelectric behaviors, benefiting from their low dark currents and high responsivities. Figure 8b shows the dependence of responsivities (1310 nm laser at power of 1 mW) on reverse bias for ITO/*n*-Ge, ITO/Al_2O_3(2 nm)/*n*-Ge and ITO/HfO_2(2 nm)/*n*-Ge diodes. It is shown that the responsivity of ITO/*n*-Ge diode approaches to a saturated value at a low reverse bias, while the responsivities of ITO/Al_2O_3(2 nm)/*n*-Ge and ITO/HfO_2(2 nm)/*n*-Ge diodes increase linearly with the increase of reverse bias. At − 4 V reverse bias, high responsivities of 12.5 A/W and 9.3 A/W are achieved for ITO/Al_2O_3(2 nm)/*n*-Ge and ITO/

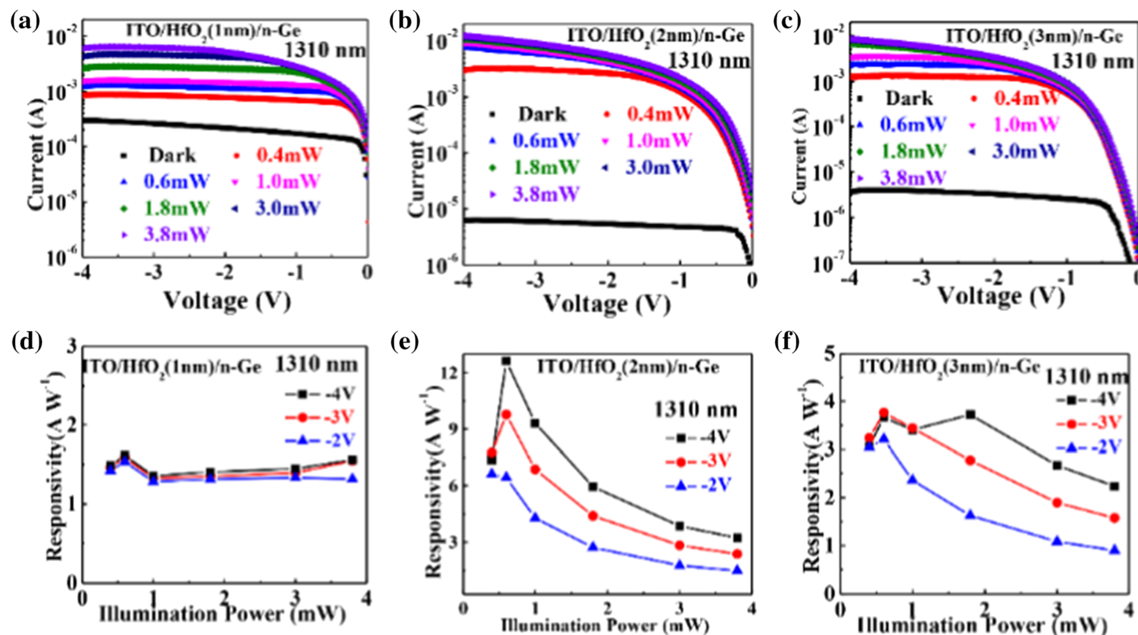

Figure 7 Photocurrent of the **a** ITO/HfO_2(1 nm)/*n*-Ge, **b** ITO/HfO_2(2 nm)/*n*-Ge and **c** ITO/HfO_2(3 nm)/*n*-Ge diodes measured under illumination with a 1310 nm laser at various powers. The illumination power dependence of responsivity of **d** ITO/HfO_2(1 nm)/*n*-Ge, **e** ITO/HfO_2(2 nm)/*n*-Ge and **f** ITO/HfO_2(3 nm)/*n*-Ge diodes measured at − 2, − 3 and − 4 V reverse bias with a 1310 nm laser.

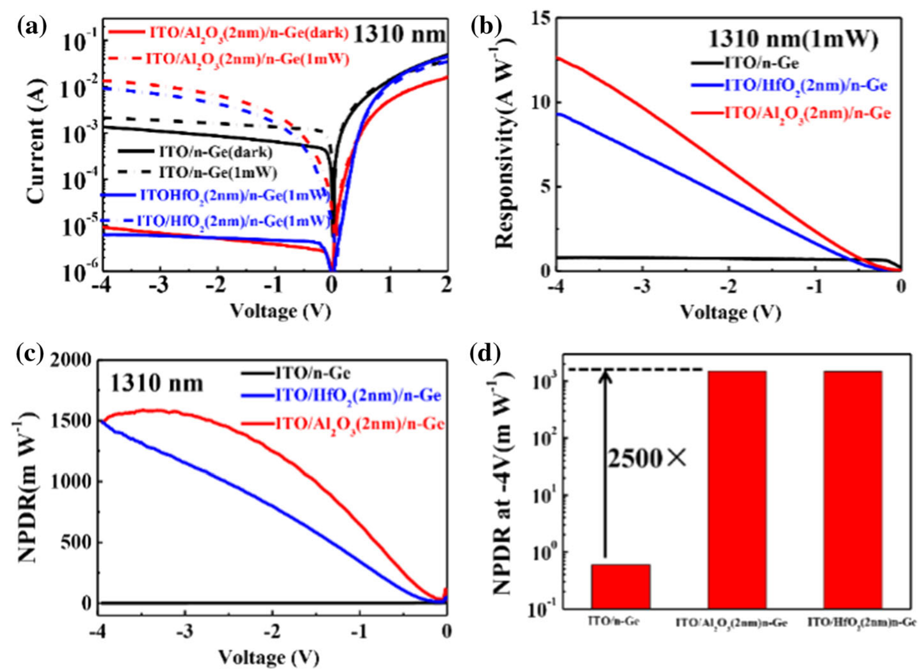

Figure 8 The comparison of **a** dark currents and photocurrents **b** responsivities **c** NPDRs and **d** NPDRs at − 4 V bias voltage, measured under illumination by a 1310 nm laser at power of 1 mW for ITO/*n*-Ge, ITO/Al_2O_3(2 nm)/*n*-Ge and ITO/HfO_2(2 nm)/*n*-Ge diodes.

HfO_2(2 nm)/*n*-Ge diodes, 16 × and 12 × higher than ITO/*n*-Ge device, respectively.

Another important performance merit for photodetectors is the normalized photo-responsivity-to-dark current ratio (NPDR) [33] defined as:

$$NPDR = R/I_{dark} \quad (2)$$

where R is the responsivity, I_{dark} is the dark current. Figure 8c shows the dependence of NPDRs (1310 nm laser at power of 1 mW) on reverse bias for ITO/*n*-Ge, ITO/Al_2O_3(2 nm)/*n*-Ge and ITO/HfO_2(2 nm)/*n*-Ge diodes. Clearly, the NPDRs of ITO/Al_2O_3(2 nm)/*n*-Ge and ITO/HfO_2(2 nm)/*n*-Ge diodes are significantly improved compared with that of ITO/*n*-Ge diode. Specially, measured at − 4 V bias voltage under illumination by a 1310 nm laser at power of 1 mW, a high NPDR of ∼ 1484 and 1488 mW^{-1} was obtained for ITO/Al_2O_3(2 nm)/*n*-Ge and ITO/HfO_2(2 nm)/*n*-Ge diode, respectively, about 2500 × higher than ITO/*n*-Ge diode, as shown in Fig. 8d.

The responsivity of the photodetector is determined by external quantum efficiency which is correlated with the number of electron–hole pairs generated per incident photon. Figure 9a shows the energy band diagram of the ITO/*n*-Ge device under light illumination. Under irradiation, at reverse bias voltage, the photogenerated electrons coming from inter-band photoemission of Ge can be transported from conduction band of Ge to back electrode. While the photogenerated holes can recombine with electrons transported from ITO electrode, at the interface between ITO and *n*-Ge. The photocurrent is upper limited by photogenerated electron–hole pairs, and thus, no photoconductive gain has been observed for ITO/*n*-Ge photodetectors.

Figure 9b shows the energy band diagram of the ITO/Al_2O_3(or HfO_2)/*n*-Ge device without light illumination. It is shown that the electrons have to overcome a high barrier height to form a dark current under reverse bias voltage. Figure 9c shows the energy band diagram of the ITO/Al_2O_3(or HfO_2)/*n*-Ge device under light illumination. Under irradiation, at reverse bias voltage, the photogenerated electrons can be transported from conduction band of Ge to back electrode as well. However, with an appropriate thickness of Al_2O_3(or HfO_2) interlayer, the recombination between photogenerated holes and electrons can be inhibited by Al_2O_3(or HfO_2) interlayer due to larger valence band offset between Al_2O_3(or HfO_2) and Ge. And the trap states existed at the surface of *n*-Ge have the possibility to be occupied by photogenerated holes. The trapped holes will cause the energy band (close to the ITO cathode) bending, which could dramatically reduce the injection barrier width for electrons to drive the electrons to tunnel through it from the ITO electrode. The quantity of injected electrons can be much larger than

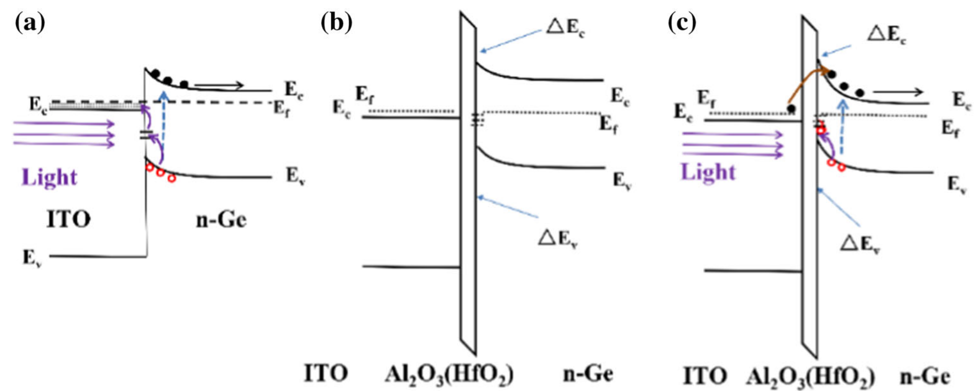

Figure 9 **a** The energy band diagram of the ITO/n-Ge device under light illumination, the energy band diagram of the ITO/Al_2O_3(or HfO_2)/n-Ge device under **b** dark and **c** light illumination.

the photogenerated ones, which should be responsible for photoconductive gain of ITO/Al_2O_3(2 nm)/n-Ge and ITO/HfO_2(2 nm)/n-Ge diodes.

The changes in responsivity for the ITO/Al_2O_3/n-Ge and ITO/HfO_2/n-Ge diodes with interlayer thickness can be explained as follows. When the interlayer thickness is very thin, the photogenerated holes can tunnel through interlayer and recombine with electrons from ITO electrode, resulting in low responsivity for ITO/Al_2O_3(1 nm)/n-Ge and ITO/HfO_2(1 nm)/n-Ge diodes. As interlayer thickness increases, tunneling behavior for photogenerated holes is inhibited, while the electrons from ITO electrode can tunnel through interlayer due to the smaller effective mass of electron and smaller $\triangle E_c$(versus $\triangle E_v$) between Al_2O_3(or HfO_2) and Ge, resulting in high responsivity for ITO/Al_2O_3(2 nm)/n-Ge and ITO/HfO_2(2 nm)/n-Ge diodes. Continuously increasing the thickness of interlayer, tunneling behavior of photogenerated electrons is inhibited, resulting in lowering responsivity for ITO/Al_2O_3(3 nm)/n-Ge and ITO/HfO_2(3 nm)/n-Ge diodes.

The dependence of responsivities for the ITO/Al_2O_3/n-Ge and ITO/HfO_2/n-Ge diodes on laser power can be explained as follows. At low laser power, the photogenerated carriers increase with laser power and are captured and converted into trapped holes, to further make the energy band bending, resulting in the improvement of responsivity for ITO/Al_2O_3/n-Ge and ITO/HfO_2/n-Ge diodes. However, continuously increasing the laser power, trap states are filled with photogenerated holes and reach saturation, and then, the recombination probability between photogenerated electrons and holes will increase, resulting in lowering responsivity for these photodiodes.

Conclusions

High photoconductive gain and low dark current ITO/Al_2O_3/n-Ge and ITO/HfO_2/n-Ge photodiodes are investigated. It is demonstrated that the introduction of an Al_2O_3 or HfO_2 interlayer can effectively increase the barrier height and suppress dark current for the ITO/n-Ge diode. Due to the surface defects states caused by Ge suboxides, Ge photodiodes with high photocurrent gain have been achieved, in which the large photoconductive gain up to 24 for 1310 nm at -9 V is obtained for ITO/Al_2O_3(2 nm)/n-Ge photodiodes. The high responsivity and low dark current of the photodiodes result in a high NPDR of 1484 and 1488 mW^{-1} for ITO/Al_2O_3(2 nm)/n-Ge and ITO/HfO_2(2 nm)/n-Ge diode, respectively, about 2500 × higher than ITO/n-Ge diode at 1310 nm under -4 V. The combination of CMOS compatibility, low dark current and high photoconductive gain at 1310 and 1550 nm makes the ITO/Al_2O_3/n-Ge and ITO/HfO_2/n-Ge photodetectors potential for a wide variety of applications in different fields.

Acknowledgements

This work was supported by National Key R&D Program of China (2018YFB2200103).

Compliance with ethical standards

Conflict of interest The authors declare that they have no conflicts of interest to this work.

References

[1] Vivien L, Polzer A, Marris-Morini D et al (2012) Zero-bias 40Gbit/s germanium waveguide photodetector on silicon. Opt Express 20(2):1096–1101

[2] Lin Y, Lee KH, Bao S, Guo X, Wang H, Michel J, Tan CS (2017) High-efficiency normal-incidence vertical pin photodetectors on a germanium-on-insulator platform. Photon Res 5(6):702–709

[3] Zhang Y, Yang S, Yang Y et al (2014) A high-responsivity photodetector absent metal-germanium direct contact. Opt Express 22(9):11367–11375

[4] Chen H, Galili M, Verheyen P et al (2016) 100-Gbps RZ data reception in 67-GHz Si-contacted germanium waveguide pin photodetectors. J Lightwave Technol 35(4):722–726

[5] Chen G, Yu Y, Deng S, Liu L, Zhang X (2015) Bandwidth improvement for germanium photodetector using wire bonding technology. Opt Express 23(20):25700–25706

[6] Hössbacher C, Salamin Y, Fedoryshyn Y et al (2017) Optical interconnect solution with plasmonic modulator and Ge photodetector array. IEEE Photon Technol Lett 29(21):1760–1763

[7] Chong L, Chun-Lai X, Ya-Ming L, Chuan-Bo L, Bu-Wen C, Qi-Ming W (2015) High performance silicon waveguide germanium photodetector. Chin Phys B24(3):423–427

[8] Dushaq G, Nayfeh A, Rasras M (2017) Metal-germanium-metal photodetector grown on silicon using low temperature RF-PECVD. Opt Express 25(25):32110–32119

[9] Zang HJ, Kim GS, Park GJ, Choi YS, Yu HY (2016) Asymmetrically contacted germanium photodiode using a metal–interlayer–semiconductor–metal structure for extremely large dark current suppression. Opt Lett 41(16):3686–3689

[10] Mukherjee S, Das K, Das S, Ray SK (2018) Highly responsive, polarization sensitive, self-biased single GeO_2-Ge nanowire device for broadband and low power photodetectors. ACS Photonics 5(10):4170–4178

[11] Philipp S, Sistani M, Greil J, Bertagnolli E, Lugstein A (2018) Ultrascaled germanium nanowires for highly sensitive photodetection at the quantum ballistic limit. Nano Lett 18(8):5030–5035

[12] Sett S, Ghatak A, Sharma DK, Kumar GVP, Raychaudhuri AK (2018) Broad band single germanium nanowire photodetectors with surface oxide-controlled high optical gain. J Phys Chem C 122(15):8564–8572

[13] Otuonye U, Kim HW, Lu WD (2017) Ge nanowire photodetector with high photoconductive gain epitaxially integrated on Si substrate. Appl Phys Lett 110(17):173104.1–173104.5

[14] Kim HS, Kumar MD, Patel M, Kim J (2016) High-performing ITO/CuO/n-Si photodetector with ultrafast photoresponse. Sens Actuators, A 252:35–41

[15] Biyikli N, Kimukin I, Aytur O, Gokkavas M, Selim Unlu M, Ozbay E (2001) 45-GHz bandwidth-efficiency resonant-cavity-enhanced ITO-Schottky photodiodes. IEEE Photonics Technol Lett 13(7):705–707

[16] Kallatt S, Nair S, Majumdar K (2018) Asymmetrically encapsulated vertical ITO/MoS_2/Cu_2O photodetector with ultrahigh sensitivity. Small 14(3):1701613–1706810

[17] Huang YT, Yeh PS, Huang YH, Chen YT, Huang CW, Lin CJ, Yeh W (2016) High-performance InGaN pin photodetectors using LED structure and surface texturing. IEEE Photonics Technol Lett 28(6):605–608

[18] Huang Z, Mao Y, Chang A et al (2018) Low-dark-current, high-responsivity indium-doped tin oxide/Au/n-Ge Schottky photodetectors for broadband 800–1650 nm detection. Appl Phys Express 11(10):102203.1–102203.5

[19] Yun JH, Kumar MD, Park YC et al (2015) High performing ITO/Ge heterojunction photodetector for broad wavelength detection. J Mater Sci: Mater Electron 26(8):6099–6106

[20] Kim H, Kumar MD, Kim J (2015) Highly-performing Ni/SiO_2/Si MIS photodetector for NIR detecting applications. Sens Actuators A Phys 233:290–294

[21] Chang PC, Chen CH, Chang SJ, Su YK, Yu CL, Huang BR, Chen PC (2006) High UV/visible rejection contrast AlGaN/GaN MIS photodetectors. Thin Solid Films 498(1):133–136

[22] Chen CH, Tsai CM, Cheng CF, Yen SF, Su PY, Tsai YH, Tsai CN (2012) GaN-based metal–insulator–semiconductor ultraviolet photodetectors with CsF current-suppressing layer. Jpn J Appl Phys 51(4S):04DG15.1–04DG15.4

[23] Kuo PS, Fu YC, Chang CC, Lee CH, Liu CW (2007) Dark current reduction of Ge MOS photodetectors by high work function electrodes. Electron Lett 43(20):1113–1114

[24] Manik PP, Lodha S (2015) Contacts on n-type germanium using variably doped zinc oxide and highly doped indium tin oxide interfacial layers. Appl Phys Express 8(5):051302.1–051302.5

[25] Sze SM, Ng KK (2008) Physics of semiconductor devices, 3rd edn. Xian Jiaotong University Press, Xi'an

[26] Tong Y, Liu B, Lim PSY, Yeo YC (2012) Selenium segregation for effective Schottky barrier height reduction in NiGe/n-Ge contacts. IEEE Electron Dev Lett 33(6):773–775

[27] Strohmeier, Brian R (1994) Characterization of an activated alumina claus catalyst by XPS. Surf Sci Spectra 3(2):141–146

[28] Oh J, Campbell JC (2004) Thermal desorption of Ge native oxides and the loss of Ge from the surface. J Electron Mater 33(4):364–367

[29] Chi X, Lan X, Chao L et al (2016) An improvement of HfO_2/Ge interface by in situ remote N2 plasma pretreatment for Ge MOS devices. Res Express 3(3):035012.1–035012.5

[30] Robertson J (2000) Band offsets of wide-band-gap oxides and implications for future electronic devices. J Vac Sci Technol B 18(3):1785–1791

[31] Huang Z, Li C, Lin G et al (2016) Suppressing the formation of GeOx by doping Sn into Ge to modulate the Schottky barrier height of metal/n-Ge contact. Appl Phys Express 9(2):021301.1–021301.4

[32] Dimoulas A, Tsipas P, Sotiropoulos A, Evangelou EK (2006) Fermi-level pinning and charge neutrality level in germanium. Appl Phys Lett 89(25):252110.1–252110.3

[33] Chi OC, Okyay AK, Saraswat KC (2003) Effective dark current suppression with asymmetric MSM photodetectors in group IV semiconductors. IEEE Photonics Technol Lett 15(11):1585–1587

Publisher's Note Springer Nature remains neutral with regard to jurisdictional claims in published maps and institutional affiliations.